nature electronics

Article

https://doi.org/10.1038/s41928-024-01219-8

An antiferromagnetic diode effect in even-layered $MnBi_2Te_4$

Received: 13 June 2023

Accepted: 12 July 2024

Published online: 12 August 2024

Check for updates

Anyuan Gao[1], Shao-Wen Chen[2], Barun Ghosh[3], Jian-Xiang Qiu[1], Yu-Fei Liu[1,2], Yugo Onishi[4], Chaowei Hu[5], Tiema Qian[5], Damien Bérubé[1], Thao Dinh[1,2], Houchen Li[1], Christian Tzschaschel[1], Seunghyun Park[2], Tianye Huang[1], Shang-Wei Lien[6,7,8], Zhe Sun[1,9], Sheng-Chin Ho[1], Bahadur Singh[10], Kenji Watanabe[11], Takashi Taniguchi[12], David C. Bell[13,14], Arun Bansil[3,15], Hsin Lin[16], Tay-Rong Chang[6,7,8], Amir Yacoby[2], Ni Ni[5], Liang Fu[4], Qiong Ma[9] & Su-Yang Xu[1] ✉

In a p–n junction, the separation of positive and negative charges leads to diode transport, in which charge flows in only one direction. Non-centrosymmetric polar conductors are intrinsic diodes that could be of use in the development of nonlinear applications. Such systems have recently been extended to non-centrosymmetric superconductors, and the superconducting diode effect has been observed. Here, we report an antiferromagnetic diode effect in a centrosymmetric crystal without directional charge separation. We observed large second-harmonic transport in a nonlinear electronic device enabled by the compensated antiferromagnetic state of even-layered $MnBi_2Te_4$. We show that this antiferromagnetic diode effect can be used to create in-plane field-effect transistors and microwave-energy-harvesting devices. We also show that electrical sum-frequency generation can be used as a tool to detect nonlinear responses in quantum materials.

Antiferromagnets (AFMs) are magnetic internally but have zero net magnetization externally. Although the internal magnetic structure does not manifest as a global magnetization, it can affect other macroscopic properties. For example, in strongly correlated systems, the antiparallel spin structure promotes virtual hopping, which makes antiferromagnetism a favourable ground state in undoped Mott insulators[1]. Alternatively, in topological physics, the internal AFM spin structures can lead to topological phases such as AFM topological insulators[2], AFM Dirac semimetals[3] and axion insulators[4]. The absence of net magnetization, combined with their fast dynamics, also makes AFMs a promising platform for spintronics[5].

Intrinsic second-order transport has been reported in non-centrosymmetric conductors[6–35]. It leads to a diode-like I–V character (for example, if $V = \alpha I + \beta I^2$, then $V(+I) \neq -V(-I)$, where α and β are coefficients). These non-centrosymmetric materials (including ferromagnetic materials) can exhibit magneto-chiral anisotropy, nonreciprocal

[1]Department of Chemistry and Chemical Biology, Harvard University, Cambridge, MA, USA. [2]Department of Physics, Harvard University, Cambridge, MA, USA. [3]Department of Physics, Northeastern University, Boston, MA, USA. [4]Department of Physics, Massachusetts Institute of Technology, Cambridge, MA, USA. [5]Department of Physics and Astronomy and California NanoSystems Institute, University of California, Los Angeles, Los Angeles, CA, USA. [6]Department of Physics, National Cheng Kung University, Tainan, Taiwan. [7]Center for Quantum Frontiers of Research and Technology (QFort), Tainan, Taiwan. [8]Physics Division, National Center for Theoretical Sciences, Taipei, Taiwan. [9]Department of Physics, Boston College, Chestnut Hill, MA, USA. [10]Department of Condensed Matter Physics and Materials Science, Tata Institute of Fundamental Research, Mumbai, India. [11]Research Center for Electronic and Optical Materials, National Institute for Materials Science, Tsukuba, Japan. [12]Research Center for Materials Nanoarchitectonics, National Institute for Materials Science, Tsukuba, Japan. [13]Harvard John A. Paulson School of Engineering and Applied Sciences, Harvard University, Cambridge, MA, USA. [14]Center for Nanoscale Systems, Harvard University, Cambridge, MA, USA. [15]Quantum Materials and Sensing Institute, Northeastern University, Burlington, MA, USA. [16]Institute of Physics, Academia Sinica, Taipei, Taiwan. ✉e-mail: suyangxu@fas.harvard.edu

https://doi.org/10.1038/s41928-024-01219-8

magnetoresistance and unidirectional magnetoresistance induced by the nonlinear Drude effect[10,11]. They can exhibit the nonlinear Hall effect without a magnetic field due to the Berry curvature dipole[9,13–15], and they can support large second-order transport without a magnetic field due to skew scattering[16,19].

Recently, a superconducting diode effect has been reported in non-centrosymmetric polar superconductors[21]. In these systems, the spatial directionality that is required for diode transport is provided by the non-centrosymmetric charge distribution. Distinct from non-centrosymmetric materials, nonlinear transport has also been reported in time-reversal breaking (magnetic) systems. Such systems can lead to the quantum metric effect, which has been observed experimentally[22,23], as well as potentially nonlinear effects in magnetic insulators and disorder scattering[24–30,32–36].

In this article, we report an AFM diode effect in a centrosymmetric crystal without directional charge separation (even-layered $MnBi_2Te_4$). The spins of an AFM generated a directional current upon a.c. excitation (Fig. 1a–c and Extended Data Fig. 1). We show that the effect can be used to create an in-plane field-effect transistor and a microwave-energy-harvesting device. We also show that electrical sum-frequency generation (SFG), which is analogous to the optical SFG previously discovered in wide-gap insulators, can be used as a tool to detect nonlinear responses in quantum materials.

AFM diode effect

A key characteristic of the AFM diode effect is that the diode direction should reverse when switching between the two opposite AFM states (AFM-I and AFM-II; Fig. 1b,c). However, due to the absence of net magnetization (Fig. 1e and Extended Data Fig. 2), it is difficult to detect and control the two opposite AFM states in a device. Moreover, many AFMs have several domains. If the numbers of domains in AFM-I and AFM-II are equal, the AFM diode effect will cancel. Therefore, to test the AFM diode effect, we need an AFM material that can be prepared as a single domain. We also need a detection method that can distinguish AFM-I and AFM-II in a device setting. Two-dimensional even-layered $MnBi_2Te_4$ is a prototypical parity–time ($\mathcal{PT}$)-symmetric AFM. Its lattice is centrosymmetric (Fig. 1d), but its AFM spins break inversion symmetry (Fig. 1b,c)[31,37–44]. Moreover, we have recently shown that optical circular dichroism (CD) can distinguish between the AFM-I and AFM-II states, even though both have zero net magnetization[45].

We fabricated devices with either Hall bar electrodes or radially distributed electrodes. They all gave consistent results as a function of AFM order, spatial direction, doping and vertical electric field. We focus here on device A, which is a six-septuple-layer (6SL) $MnBi_2Te_4$ sample with radially distributed electrodes (Fig. 1f) and dual gating. The dual gating allows us to simultaneously control the carrier density n_e and the vertical electric field E_z. All measurements were performed without a magnetic field at $T = 1.7$ K unless otherwise noted. We start by considering the d.c. longitudinal I–V characteristics. We observed a clear diode behaviour, as shown in Fig. 1g, with a larger resistance in one direction but a smaller resistance in the opposite direction. We subtracted the linear background from our I–V data. The difference (inset of Fig. 1g) shows clear quadratic behaviour $\Delta V = V - \alpha I = \beta I^2$. Therefore, this diode effect is characterized by second-order nonlinear transport. Such nonlinear transport can be measured by the lock-in technique, for which we inject an a.c. current I^ω and probe the second-harmonic voltage $V^{2\omega}$ (Fig. 1h).

Next, we performed simultaneous optical and electrical measurements. Optically, we used the CD to confirm that our 6SL $MnBi_2Te_4$ was, indeed, in a single-domain state[45]. Then, electrically, we detected the nonlinear transport signal to search for the AFM diode effect. As demonstrated by previous experiments, the $\mathcal{PT}$-symmetric AFM order can be controlled by the $\mathbf{E} \cdot \mathbf{B}$ field[42,46]. We followed the established procedures[42]. Under a fixed vertical electric field ($E_z = -0.2$ V nm^{-1}), we swept the vertical magnetic field ($\mu_0 H_z$) from −8 to 0 T to prepare AFM-I (Fig. 2a) and from +8 to 0 T to prepare AFM-II (Fig. 2b and Extended Data Fig. 3). To prove that we had, indeed, prepared a single-domain AFM state, we measured the spatially resolved CD. As mentioned above, a $\mathcal{PT}$-symmetric AFM with zero net magnetization can support AFM CD in the reflection channel[45,47], such that the signal is opposite between AFM-I and AFM-II. As shown in Fig. 2c,d, the entire sample has the same CD signal. We then measured the longitudinal nonlinear transport signals for such single-domain AFM states. Our data (Fig. 2e,f and Extended Data Fig. 4) show that the two AFM states feature opposite longitudinal nonlinear voltages $V_{\parallel}^{2\omega}$. Hence, they exhibit opposite diode effects. By contrast, the longitudinal linear voltages (the regular resistances) shown in Extended Data Fig. 3 are the same for the two AFM states. We also measured the second-harmonic conductivity ($\sigma^{2\omega}$) while increasing the temperature. Shown in Extended Data Fig. 5, the nonlinear signal disappears above the Néel temperature $T_N \simeq 21$ K.

Therefore, our data show that the single-domain AFM state in 6SL $MnBi_2Te_4$ exhibits a clear nonlinear transport signal. Its sign depends on the AFM state. Hence, the observed nonlinear effect directly arises from the inversion breaking of the AFM spin structure, which is opposite for AFM-I and AFM-II. This finding is equivalent to the nonlinear

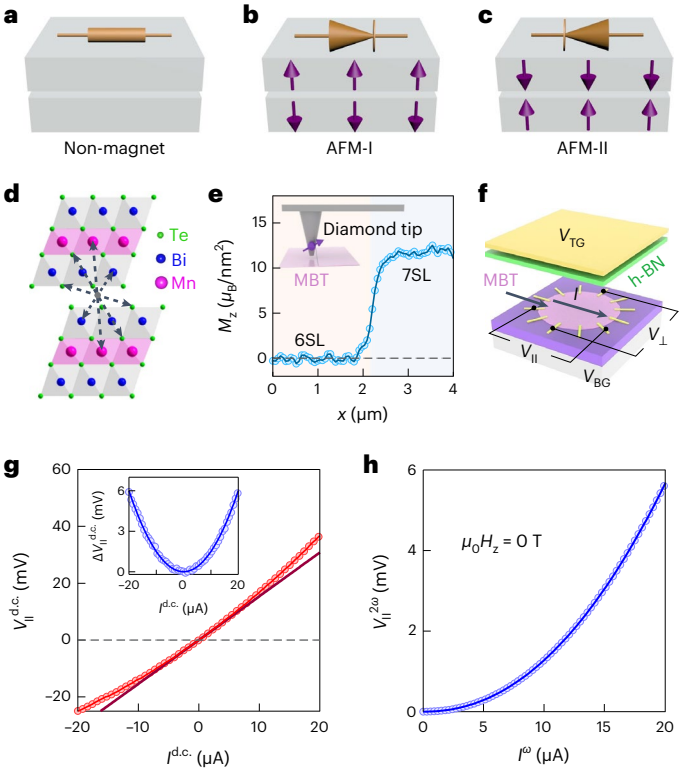

Fig. 1 | Introduction to $\mathcal{PT}$-symmetric antiferromagnetism in even-layered $MnBi_2Te_4$. **a**–**c**, Schematic illustration showing the AFM diode effect. In a non-magnetic crystal with a centrosymmetric lattice, the diode effect is absent (**a**). The introduction of AFM spin into the lattice breaks the inversion symmetry, resulting in the AFM diode effect (**b**). After reversing the AFM states from AFM-I to AFM-II, the diode signal also reverses its sign (**c**). **d**, Lattice of an even-layered $MnBi_2Te_4$ flake (bilayer used as an example). The lattice is centrosymmetric with the inversion centre between the two layers. **e**, NV measurement of a $MnBi_2Te_4$ flake. The magnetization (M_z) in 6SL $MnBi_2Te_4$ was negligible. x is the length of the line scan. **f**, Schematic illustration of an even-layered $MnBi_2Te_4$ (MBT) device with dual gating. V_{BG} and V_{TG} are the top and bottom gate voltages, respectively. $V_\parallel$ and $V_\perp$ are the voltages probed along the longitudinal and transverse directions of the applied current (I). **g**, d.c. I–V characteristic of our 6SL $MnBi_2Te_4$ device. We subtracted a linear background (V) from the measured longitudinal voltage $V_\parallel^{d.c.}$. The resulting $\Delta V_\parallel^{d.c.}$ (inset) shows quadratic behaviour. $I^{d.c.}$ is the d.c. bias current. **h**, a.c. I–V characteristic of the 6SL $MnBi_2Te_4$ device. We injected a current with frequency ω (I^ω) and recorded the 2ω frequency longitudinal voltage ($V_\parallel^{2\omega}$) at zero external magnetic field ($\mu_0 H_z = 0$). 7SL, seven-septuple-layer sample.

https://doi.org/10.1038/s41928-024-01219-8

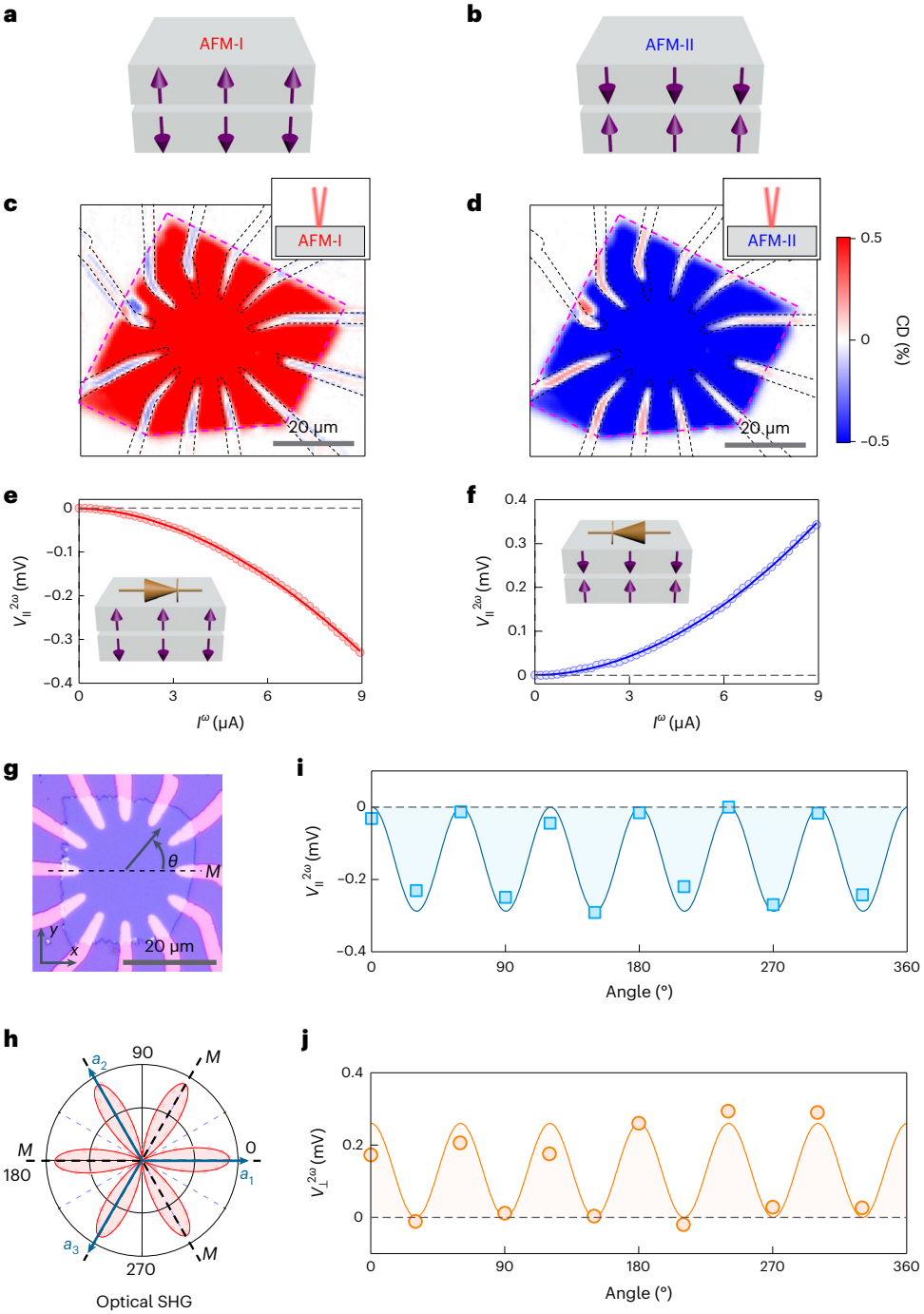

Fig. 2 | Observation of the antiferromagnetic diode effect. a,**b**, Schematic of AFM-I (**a**) and AFM-II (**b**), which can be prepared by sweeping the magnetic field under a fixed electric field following the procedures established by previous works[42] (Extended Data Fig. 3). **c**,**d**, As shown by our recent work[45], a $\mathcal{PT}$-symmetric AFM with zero net magnetization can support non-zero CD in the reflection channel (the AFM CD), whose sign is opposite for AFM-I (**c**) and AFM-II (**d**). Therefore, our spatial mapping of the reflection CD shows that our 6SL $MnBi_2Te_4$ device has been prepared in a single-domain AFM state depending on the preparation procedure, as explained in Extended Data Fig. 3. The colour legend shows the value of CD = $\frac{\sigma^L-\sigma^R}{\sigma^L+\sigma^R}$, where σ^L and σ^R are the reflected light intensities of left and right circularly polarized light, respectively. **e**,**f**, Nonlinear longitudinal voltage ($V_{\parallel}^{2\omega}$) as a function of incident current (I^{ω}) for AFM-I (**e**) and AFM-II (**f**). **g**,**h**, We determined the crystalline axes of device A by optical SHG (**h**). The non-zero SHG regions are shaded to make them more noticeable. We deliberately aligned the electrodes with the crystalline axes (**g**). The dashed lines labelled $\mathcal{M}$ denote the mirror line of $MnBi_2Te_4$. a_1, a_2 and a_3 are the three crystalline axes of $MnBi_2Te_4$. **i**,**j**, Angular dependence of the longitudinal (**i**) and transverse (**j**) nonlinear voltages as the direction of the current is varied. These data was taken at I^{ω} = 8 μA.

conductivity σ_{ijk}^{NL}, where i, j and k are laboratory coordinate axes (the first subscript i is the measurement direction and the next two subscripts j and k are the bias directions), being odd under a time-reversal operation, a hallmark of the AFM diode effect: $\sigma_{ijk}^{NL} = \frac{J_i^{2\omega}}{E_j^{\omega}E_k^{\omega}} = \frac{V_i^{2\omega}}{I_j^{\omega}I_k^{\omega}R^3}\frac{l^2}{wd}$, where R is the sample resistance, $J_i^{2\omega}$ is the second-harmonic electric current density in the j direction, E_j^{ω} and E_k^{ω} are the electric fields in the j and k directions, I_j^{ω} and I_k^{ω} are the currents in the j and k directions, and l, w and d are the sample length, width and thickness.

https://doi.org/10.1038/s41928-024-01219-8

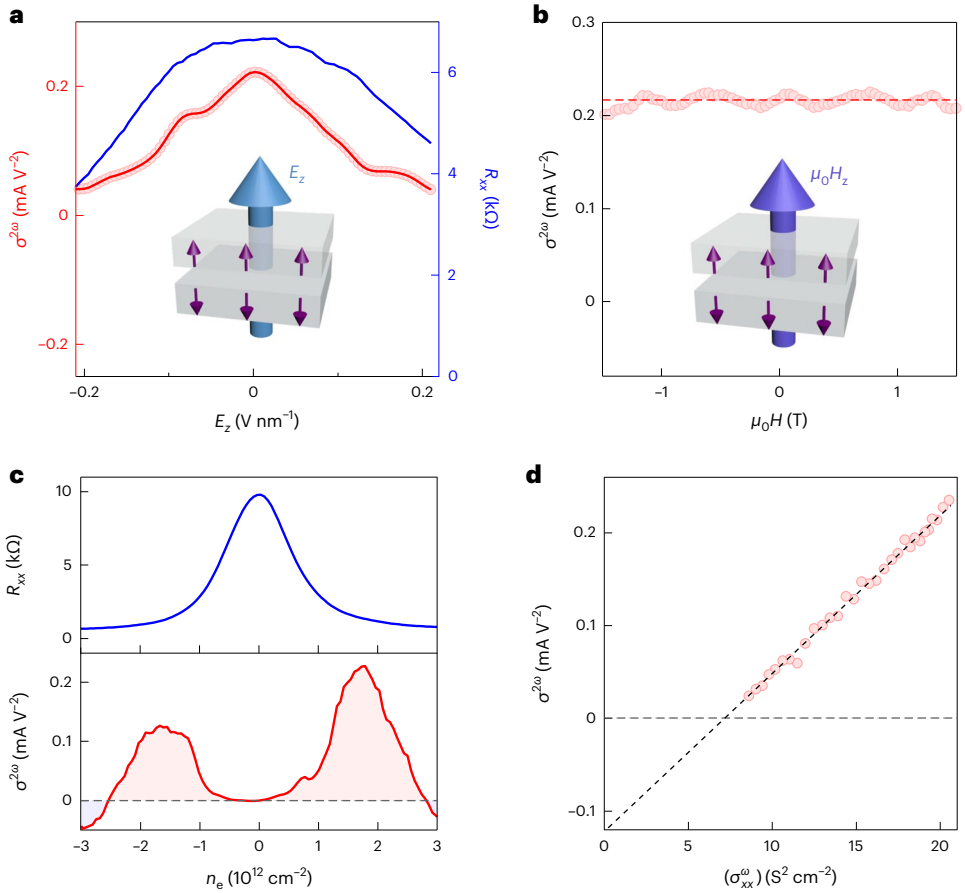

Fig. 3 | Systematic investigations of the intrinsic antiferromagnetic diode effect. a, Nonlinear conductivity $\sigma^{2\omega}$ and longitudinal resistance R_{xx} as functions of the vertical electric field E_z. **b**, Nonlinear conductivity as a function of the vertical magnetic field $\mu_0 H_z$ in the AFM state. The red dashed line is the average line of $\sigma^{2\omega}$. **c**, Experimentally measured longitudinal resistance (upper panel) and nonlinear conductivity (lower panel) as functions of charge density n_e. The positive and negative $\sigma^{2\omega}$ regions are shaded pink and light blue, respectively. **d**, Scaling between the nonlinear conductivity and the square of the regular linear conductivity. The dark dashed line is the linear fit to the scaling curve.

Systematic studies of the intrinsic AFM diode effect

To further confirm that the nonlinear signal is an intrinsic effect of the AFM, we study how the nonlinear signal depends on the crystallographic directions. We deliberately aligned the electrodes in device A with the crystalline axes (Fig. 2g), which were determined by optical second-harmonic generation (SHG; Fig. 2h). These preparations allowed us to test the dependence of the nonlinear signal on the crystalline direction. The longitudinal nonlinear signal oscillated between zero and non-zero, respecting the threefold rotational symmetry of the $MnBi_2Te_4$. In addition to the longitudinal nonlinear signal, we actually also detected a transverse nonlinear signal. Later in this paper (Fig. 4), we will study the exchange property to differentiate this transverse diode signal from a nonlinear Hall effect. Here, we focus on the crystallographic directional dependence. By comparing Fig. 2i,j, we can observe the following: the longitudinal second-harmonic voltage $V^{2\omega}_{\parallel}$ was zero when the current was parallel to a crystalline axis (dotted lines in Fig. 2h) but a maximum when the current was perpendicular. By contrast, the transverse second-harmonic voltage $V^{2\omega}_{\perp}$ had the opposite directional dependence: $V^{2\omega}_{\perp}$ was a maximum when the current was parallel to a crystalline axis but zero when the current was perpendicular (Extended Data Fig. 6).

This directional dependence can help us to understand the nature of the observed nonlinear signals (whether they intrinsically obey the symmetry of the AFM order or are artefact due to device imperfection or asymmetry). If the signals are an intrinsic response of the AFM state of even-layered $MnBi_2Te_4$, the nonlinear signals and their directional dependence should be consistent with the symmetry of the AFM state, which is $-3'm'$ for even-layered $MnBi_2Te_4$. Through symmetry analysis, one can show that the group $-3'm'$ dictates that $\sigma^{NL}_{yxx} = -\sigma^{NL}_{yyy}$ are non-zero but $\sigma^{NL}_{xxx} = \sigma^{NL}_{xyy} = 0$, consistent with our data, which, therefore, strongly suggests that our observed nonlinear signals are intrinsic.

We performed further systematic studies. Figure 3a shows the dependence of the nonlinear conductivity $\sigma^{2\omega}$ on E_z, from which we see that $V^{2\omega}$ in our $MnBi_2Te_4$ system did not require a finite electric E_z field. Because E_z led to a finite electric polarization $P_z = \chi_e E_z$, where χ_e is the electric polarizability, equivalently, our system supports nonlinear transport even though it has zero electric polarization ($P_z = 0$). Figure 3b shows the dependence of $V^{2\omega}$ on $\mu_0 H_z$, from which we see that $V^{2\omega}$ in our system also did not require a finite magnetic field. Therefore, the observed nonlinear signal was not induced by the external electric or magnetic field. Figure 3c shows the dependence of $\sigma^{2\omega}$ on charge density n_e. To uncover further information about the microscopic mechanisms, we studied the dependence of $\sigma^{2\omega}$ on relaxation time τ by measuring the scaling between $\sigma^{2\omega}$ and the linear Drude conductivity σ^{ω}_{xx} through the temperature dependence. Our data (Fig. 3d and Extended Data Fig. 5) show that the nonlinear conductivity $\sigma^{2\omega}$ has two components, one proportional to τ^2 and the other proportional to τ^0 ($\sigma^{2\omega} = a_0\tau^0 + a_2\tau^2$, where a_0 and a_2 are coefficients). The existence of two components suggests that there are several coexisting microscopic mechanisms. Based on theoretical studies of nonlinear transport in AFMs[25–30,32–35], we propose that the τ^2 component can arise from the nonlinear Drude effect and disorder scattering[30,34,35], whereas the τ^0

https://doi.org/10.1038/s41928-024-01219-8

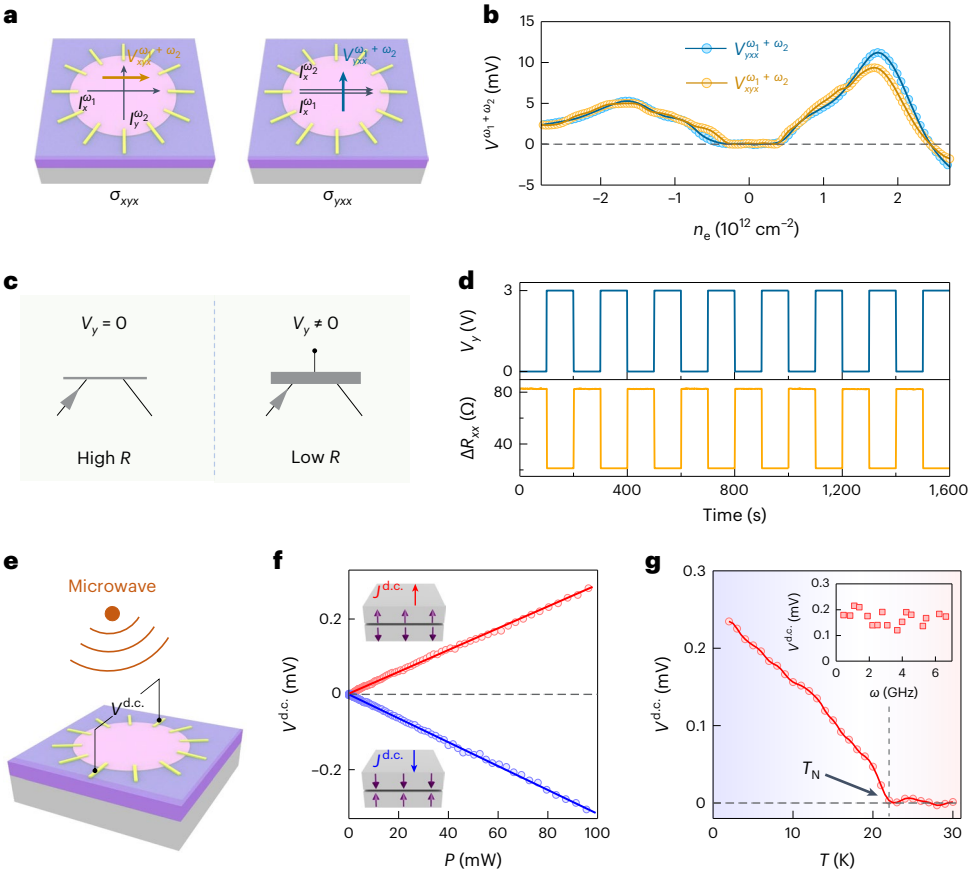

Fig. 4 | SFG measurements and applications of the AFM diode effect. **a**, Schematic of the SFG measurements. We inject two currents with different frequencies (I^{ω_1} and I^{ω_2}) and probe the SFG voltage $V^{\omega_1+\omega_2}$ (see Methods and Extended Data Fig. 9 for technical details). This electrical SFG is particularly advantageous for studying nonlinear conductivity σ^{NL}_{xyx} (where the first subscript is the probe direction and the next two subscripts are the applied current directions). The two currents have different frequencies, making it feasible to inject them along different directions. **b**, V^{NL}_{xyx} and V^{NL}_{yxx} measured using the SFG measurement method. The SFG signal is symmetric upon exchanging the first two indices of V^{ND}_{ijk}, which is consistent with the AFM group $-3'm'$ of $MnBi_2Te_4$. **c**, SFG realizes an intrinsic in-plane field effect. When we take $\omega_2 \to 0$, the SFG experiment becomes $J^{\omega_1}_x = \sigma^{NL}_{xyx} E^{d.c.}_y \cdot E^{\omega_1}_x$ (where $E^{d.c.}_y$ is the d.c. electric field in the y direction, and $E^{\omega_1}_x$ is the a.c. electric field with frequency ω in the x direction). This equation can be further rewritten as $J^{\omega_1}_x = \Delta\sigma_{xx} E^{\omega_1}_x$, where $\Delta\sigma_{xx} \propto \sigma^{NL}_{xyx} E^{d.c.}_y$. In other words, the conductance or resistance along x can be directly modulated by an electric field bias along y. **d**, Measured change of resistance R_{xx} ($\Delta R_{xx} = V^{\omega_1}_x / I^{\omega_1}_x$) as a function of an electric field bias along V_y. **e**, Schematic illustration of the wireless microwave radiation harvesting. **f**, Measured d.c. rectification voltage as a function of the wireless electromagnetic power (P) for both AFM states. **g**, Measured d.c. rectification voltage as a function of temperature. The inset shows the d.c. rectification voltage as a function of frequency ω.

component may arise from the quantum metric and disorder scattering[34,35]. We directly computed the nonlinear Drude conductivity based on the intrinsic band structure of 6SL $MnBi_2Te_4$ (Extended Data Fig. 7c). Their difference suggests that beyond nonlinear Drude, the quantum metric and disorder scattering could also have made important contributions to our data. Note that, in contrast to the well-known nonlinear Drude effect, the quantum metric and disorder scattering are still under active theoretical investigation[25–30,32–34]. Our current data are insufficient to isolate the contribution of the quantum metric from contributions induced by disorder scattering. It would be interesting to measure the nonlinear conductivity of pristine $MnBi_2Te_4$ at terahertz frequencies ($\omega\tau \gg 1$), at which the disorder scattering may be suppressed[48].

Electrical SFG by AFM spins

We now report electrical SFG in our $MnBi_2Te_4$ devices. Although optical SFG is well known, electrical SFG has rarely been studied. We show that electrical SHG can be used to study the exchange property, which can be used to differentiate our transverse diode signal from a nonlinear Hall effect. To demonstrate the importance of the exchange property, we first give an example of linear conductivity, namely a simple 2×2 tensor $\begin{pmatrix} \sigma_{xx} & \sigma_{xy} \\ \sigma_{yx} & \sigma_{yy} \end{pmatrix}$ in two dimensions. There are two distinctly different physical mechanisms for non-zero transverse linear conductance: (1) the Hall effect and (2) crystalline anisotropy. These two distinctly different kinds of transverse linear conductance are differentiated by their exchange properties. The Hall effect is antisymmetric, $\sigma_{xy} = -\sigma_{yx}$. By contrast, anisotropy-induced transverse conductance is symmetric, $\sigma_{xy} = \sigma_{yx}$ (Extended Data Fig. 8a,b).

The same logic can be applied to nonlinear conductivity. Our observation of a transverse nonlinear voltage means that σ^{NL}_{yxx} is non-zero. However, to understand its origin, we studied the exchange property (Extended Data Fig. 8c,d), that is, we compared σ^{NL}_{yxx} and σ^{NL}_{xyx}. If $\sigma^{NL}_{yxx} = -\sigma^{NL}_{xyx}$ (antisymmetric), then the transverse nonlinear signal is a nonlinear Hall effect[18]. By contrast, if $\sigma^{NL}_{yxx} = \sigma^{NL}_{xyx}$ (symmetric), then it is not a Hall effect. Rather, it is an AFM diode effect just like the longitudinal component.

Measuring σ^{NL}_{xyx} in an electrical SHG experiment, however, is difficult, because it requires passing one current I^{ω} along x and another I^{ω} along y without undesired interference. As such, to isolate and study σ^{NL}_{xyx}, we present a measurement that was unachieved previously, electrical SFG. We injected two currents with different frequencies (I^{ω_1} and I^{ω_2})

and probed the SFG voltage $V^{\omega_1+\omega_2}$. (We needed to set $\omega_1 \gg \omega_2$ to achieve the electrical SFG measurements. See Methods for technical details.) Electrical SFG is particularly advantageous for studying σ^{NL}_{xyx}. The two currents have different frequencies, so clearly separating their trajectories along orthogonal directions is feasible (Extended Data Fig. 9 and Methods). As shown in Fig. 4a,b, our sample indeed supported strong SFG $V^{\omega_1+\omega_2}_{xyx}$ by injecting currents along both the x and y directions. Moreover, we used this SFG method to measure both σ^{NL}_{xyx} and σ^{NL}_{yxx}. In our data $\sigma^{NL}_{xyx} = \sigma^{NL}_{yxx}$, which shows that our transverse nonlinear signal was not a Hall effect. Rather, it was an AFM diode effect, just like the longitudinal component. More broadly, our SFG measurement establishes a universal method for studying the nonlinear electrical transport processes of quantum materials and can be applied to many other systems.

In-plane field-effect transistor and AFM harvesting of wireless radiation

The σ^{NL}_{xyx} realized an intrinsic in-plane field-effect transistor (Fig. 4c and Extended Data Fig. 10) and potentially an electro-optical modulator. To see this, let us take $\omega_2 \to 0$. Then the SFG experiment evolves into $\Delta J^{\omega_1}_x = \sigma^{NL}_{xyx} E^{d.c.}_y E^{\omega_1}_x = \Delta\sigma_{xx} E^{\omega_1}_x$. Hence, we have $\Delta\sigma_{xx} = \sigma^{NL}_{xyx} E^{d.c.}_y$. In other words, the conductance or resistance along x can be directly modulated by an electric field bias along y. In Fig. 4c,d, we applied an a.c. bias along x and a d.c. bias along y. By turning the d.c. bias along y on and off, we, indeed, observed a clear change of resistance along x, therefore demonstrating the in-plane field effect. In traditional field-effect transistors, the electric field is supplied by the gate along the out-of-plane direction. In many cases, the capacitance of gate dielectrics is the bottleneck limiting its on/off speed. By contrast, in our case, gating is not needed, as the electric field is supplied by a bias across two contacts along the in-plane direction. This in-plane field effect can potentially enable ultrafast transistors. Further increasing ω_1 to terahertz range could potentially realize an electro-optical modulator, such that the optical conductivity (the dielectric constant) of the terahertz light can be modulated by the d.c. bias $E^{d.c.}_y$. Whereas the known electro-optic effect occurs in insulators, the effect envisioned here arises from a Fermi surface contribution.

In addition to SHG and SFG, the second-order transport also enables rectification. We demonstrated the rectification of wireless microwave radiation into d.c. electricity based on the AFM diode effect. As shown in Fig. 4e, wireless microwaves were irradiated onto the device from free space (Methods). A d.c. electric voltage that was linear to the microwave power (hence, quadratic to the microwave electric field) was observed (Fig. 4f). Moreover, the d.c. signal could be directly switched by reversing the AFM order (Fig. 4f). The rectification had a broadband response (inset of Fig. 4g), including at Wi-Fi frequencies (2.4 and 5 GHz). As such, our data demonstrates a wireless rectification device that can be controlled by the AFM spins.

Conclusions

We have reported intrinsic spin-induced nonlinearity in $\mathcal{PT}$-symmetric AFM conductors. This was achieved using a spatially resolved optical method (AFM CD) to determine that we had a single AFM domain, using electrical SFG measurements to determine that the nonlinear conductivity studied in the pristine $MnBi_2Te_4$ was indeed symmetric and determining that systematic dependences as functions of temperature, spatial direction, AFM domain, E field and $\mu_0 H$ field were all consistent with the intrinsic magnetic group of the AFM order of $MnBi_2Te_4$ ($-3'm'$). We have also shown that electrical SFG measurements, which are analogous to the optical SFG previously discovered in wide-gap insulators, can be used as a tool to detect nonlinear responses in quantum materials.

For strongly correlated materials, our AFM diode effect is a sensitive probe of the exotic $\mathcal{PT}$-symmetric order parameter of Fermi surface electrons such as the loop current (pseudo-gap) states[31,49,50]. Our approach could be used to develop new device concepts, such as AFM logic circuits, AFM-based microwave harvesters and self-powered AFM spintronic devices. In the future, the identification of room-temperature AFM materials with large nonlinear responses could also potentially lead to approaches that combine AFM spintronics, nonlinear electronics and topological materials.

Methods

Bulk crystal growth

Our $MnBi_2Te_4$ bulk crystals were grown by the Bi_2Te_3 flux method[51]. Elemental Mn, Bi and Te were mixed at a molar ratio of 15:170:270, loaded into a crucible and sealed in a quartz tube under Ar at one-third atmospheric pressure. The ampule was first heated to 900 °C for 5 h. It was then moved to another furnace where it slowly cooled from 597 °C to 587 °C and kept at 587 °C for 1 d. Finally, $MnBi_2Te_4$ was obtained by centrifuging the ampule to separate the crystals from the Bi_2Te_3 flux.

Sample fabrication

Owning to the sensitive chemical nature of $MnBi_2Te_4$ flakes, all fabrication processes were completed in an argon environment without exposure to air, chemicals or heat. An argon-filled glovebox was maintained at O_2 and H_2O levels below 0.01 ppm and a dew point below −96 °C. The glovebox was attached to an e-beam evaporator, allowing us to deposit metal without exposure to air. $MnBi_2Te_4$ was mechanically exfoliated onto a baked 300 nm SiO_2/Si wafer using Scotch Magic tape. $MnBi_2Te_4$ flakes with straight edges were deliberately chosen, as the straight edges were probably along the crystalline direction. After scratching a flake into a rectangular or circular shape with a tip, a stencil mask technique[42] was used to make Cr/Au contacts on top of the $MnBi_2Te_4$ without exposing it to air or chemicals. Hexagonal boron nitride (h-BN) flakes were directly exfoliated onto a polydimethylsiloxane film, and a 10–30-nm-thick h-BN flake was identified and transferred onto the $MnBi_2Te_4$ as the top gate dielectric layer. Next, a metal gate was evaporated onto the h-BN/$MnBi_2Te_4$ heterostructure. The contacts were aligned along the straight edges of the $MnBi_2Te_4$. To check the angle between a contact and the $MnBi_2Te_4$ crystalline direction, optical SHG measurements were performed on the sample after the transport measurements were done. The h-BN and top gate were removed using bluetape (Ultron Systems, Inc. P/N: 1007R-6.0) before the SHG measurements. This approach ensured that the $MnBi_2Te_4$ flakes were fresh for transport measurements.

Optical SHG measurements

All optical SHG experiments were performed using a near-infrared femtosecond laser at room temperature. The light source was an amplified Yb:KGW laser (Pharos, LightConversion) emitting 168 fs pulses at 1.2 eV with a pulse energy of 100 μJ and a default repetition rate of 100 kHz. All measurements were performed at normal incidence. The polarization of the incident laser was controlled using an achromatic half-wave plate, while a Glan-laser polarizer prism was used as an analyser to select the polarization of the outgoing SHG signal. Both the half-wave plate and the Glan-laser prism were mounted on motorized rotation stages. At room temperature, the crystal structure in the interior of a thin $MnBi_2Te_4$ flake is centrosymmetric (group D_{3d}). Therefore, the SHG signals were expected to originate only from the surface (surface group C_{3v}). These results are consistent with previous SHG results with Bi_2Se_3 (same symmetry as $MnBi_2Te_4$ above T_N)[52].

Optical CD measurements

Optical CD measurements were performed in a closed-loop magneto-optical cryostat (OptiCool, Quantum Design; base temperature ~2 K and B field ±7 T) using a supercontinuum laser (SuperK Extreme, NKT Photonics; wavelength 500 to 2,500 nm, pulse width 12 ps at 1,064 nm). A spectrometer (SpectraPro-300i, Acton Research) was used to select the wavelength. The wavelength used for the CD

measurement was 946 nm. The beam went through a photoelastic modulator operating at $\lambda/4$ retardation with a frequency of 50 kHz. After an optical chopper (1,000 Hz), the beam was focused onto the sample by a super apochromatic objective (Mitutoyo; numerical aperture of 0.42). The reflected beam went through the cryostat's top window, was collimated by the same objective and was collected by an avalanche photodiode. The corresponding reflected signal from the avalanche photodiode was analysed by two lock-in amplifiers at 50 kHz (the photoelastic modulator frequency) and 1,000 Hz (the chopper frequency), respectively. The CD was the ratio of the 50 kHz and 1,000 Hz signals. Spatial imaging was achieved using a scanning mirror galvanometer.

Nitrogen-vacancy measurements

The magnetization of 6SL and seven-septuple-layer $MnBi_2Te_4$ flakes was measured with a home-built scanning nitrogen-vacancy (NV) magnetometry microscope at a base temperature of 4 K and in a He_4 vapour environment. The set-up is described in ref. 53. A flake was field-cooled and measured with an external field aligned with the NV axis (out-of-plane field of 80 mT and in-plane field of 140 mT). The NV centre measures the static magnetic field generated by the odd-layered ferromagnetic flake at a stand-off height of about 100 nm. The magnetization was reconstructed with the Fourier transform method, which is like the method described in ref. 54.

Nonlinear electrical transport measurements

Electrical transport measurements were carried out with a physical properties measurement system (Quantum Design DynaCool). The base temperature was 1.65 K, and the maximum magnetic field was 9 T. The gate voltages were applied by Keithley 2400 source meters. Longitudinal and transverse voltages were measured simultaneously. Both first- and second-harmonic signals were collected by standard lock-in techniques (Stanford Research Systems Model SR830) with excitation frequencies between 1 and 600 Hz.

SFG measurements

For the SFG measurements, we injected two currents with frequencies ω_1 and ω_2 and detected the SFG voltage $V^{\omega_1+\omega_2}$. By separating the two currents in the frequency domain, it is easier to control their directions separately. The SFG voltage can be expressed as $V^{\omega_1+\omega_2} \propto \sin(\omega_1+\omega_2)t$. Standard lock-in detectors (SR830) cannot directly lock to the $\omega_1+\omega_2$ frequency. Instead, we measured $\sin\omega_1 t \sin\omega_2 t$, which directly relates to $\sin(\omega_1+\omega_2)t$ by the angle addition theorem. We chose $\omega_1 = 547.1$ Hz and $\omega_2 = 1.77$ Hz, so that $\omega_1 \gg \omega_2$. To properly define the current trajectories of the ω_1 current and ω_2 current, a 40 H inductor and 1 µF capacitor were used. To probe $\sin\omega_1 t \sin\omega_2 t$, the SFG voltage signal was fed to the first lock-in amplifier (A), which was locked to ω_1, and its integral time was set to $2\pi/w_1 < t_1 \ll 2\pi/w_2$. The output was then fed to the second lock-in amplifier (B), which was locked to ω_2, and its integral time was set to $t_2 > 2\pi/w_2$. The output of the second lock-in amplifier was $\sin\omega_1 t \sin\omega_2 t$. The measurement set-ups for $\sigma_{yxx}^{2\omega}$ and $\sigma_{xyx}^{2\omega}$ are shown in Extended Data Fig. 9.

In-plane field-effect measurements

The in-plane field-effect experiments were like the SFG measurements except that $\omega_2 \to 0$. The d.c. signal was applied by a Keithley 2400 source meter along y, and the ω_1 signal was applied by a lock-in amplifier along x. To properly define the trajectories of the d.c. current and the ω_1 current, we connected a 40 H inductor in series in the d.c. current loop before grounding, and a 1 µF capacitor in series in the ω_1 current loop before grounding. The in-plane field-effect voltage $V_x^{\omega_1}$ can be expressed as $V_x^{\omega_1} = R_{xyx}I_x^{\omega_1}I_y^{\mathrm{d.c.}} = (R_{xyx}I_y^{\mathrm{d.c.}})I_x^{\omega_1} = \Delta R_{xx}I_x^{\omega_1}$, where $\Delta R_{xx} = R_{xyx}I_y^{\mathrm{d.c.}}$. The chiral inner product was small in the near d.c. transport regime. $V_x^{\omega_1}$ was directly recorded by standard lock-in detectors. The in-plane field-effect resistance ΔR_{xx} was calculated by $\Delta R_{xx} = V_x^{\omega_1}/I_x^{\omega_1}$, which can be modulated by $I_y^{\mathrm{d.c.}}$ (Fig. 4d).

Wireless radio-frequency rectification measurements

We set up a simple experiment to harvest wireless radio-frequency (RF) signals and record the generated d.c. signals. The RF signal generator was Hittite HMC-T2220. The samples were connected to a low-temperature probe. The RF signals went into the low-temperature probe through a coaxial cable. The other end of the coaxial cable was connected to an antenna, which was made from a 50-mm-long conducting wire with a diameter of ~0.2 mm. The end of the antenna was parallel to the sample, and the spacing was ~10 mm. The electrical field direction and power of the RF signals shone on the sample were not well defined. The d.c. voltage signals were recorded by digital multimeters (Agilent 34401A).

Density functional theory calculations

Ab initio calculations based on density functional theory were performed using the projector augmented-wave pseudopotentials and a plane-wave basis set as implemented in the VASP package. Spin–orbit coupling was included following the standard implementation in the VASP package[55]. A $9 \times 9 \times 1$ Γ-centred k-grid was used for the Brillouin zone integration. The kinetic energy cutoff for the plane-wave basis was set to 400 eV. The generalized gradient approximation scheme with an on-site Coulomb potential ($U = 5.0$ eV) was used for the localized Mn 3d orbitals[56]. The Wannier function-based tight binding model was built using the Wannier90 code[57].

Data availability

Source data are provided with this paper. Further data related to this work are available from the corresponding authors upon request.

Code availability

The computer code used in this study is available from the corresponding authors upon reasonable request.

References

1. Lee, P. A., Nagaosa, N. & Wen, X.-G. Doping a Mott insulator: physics of high-temperature superconductivity. *Rev. Mod. Phys.* **1**, 17–84 (2006).
2. Mong, R. S., Essin, A. M. & Moore, J. E. Antiferromagnetic topological insulators. *Phys. Rev. B* **81**, 245209 (2010).
3. Tang, P., Zhou, Q., Xu, G. & Zhang, S.-C. Dirac fermions in an antiferromagnetic semimetal. *Nat. Phys.* **12**, 1100–1104 (2016).
4. Essin, A. M., Moore, J. E. & Vanderbilt, D. Magnetoelectric polarizability and axion electrodynamics in crystalline insulators. *Phys. Rev. Lett.* **102**, 146805 (2009).
5. Jungwirth, T., Marti, X., Wadley, P. & Wunderlich, J. Antiferromagnetic spintronics. *Nat. Nanotechnol.* **11**, 231–241 (2016).
6. Rikken, G., Fölling, J. & Wyder, P. Electrical magnetochiral anisotropy. *Phys. Rev. Lett.* **87**, 236602 (2001).
7. Tokura, Y. & Nagaosa, N. Nonreciprocal responses from non-centrosymmetric quantum materials. *Nat. Commun.* **9**, 3740 (2018).
8. Orenstein, J. et al. Topology and symmetry of quantum materials via nonlinear optical responses. *Annu. Rev. Condens. Matter Phys.* **12**, 247–272 (2021).
9. Sodemann, I. & Fu, L. Quantum nonlinear Hall effect induced by Berry curvature dipole in time-reversal invariant materials. *Phys. Rev. Lett.* **115**, 216806 (2015).
10. Ideue, T. et al. Bulk rectification effect in a polar semiconductor. *Nat. Phys.* **13**, 578–583 (2017).
11. Yasuda, K. et al. Large unidirectional magnetoresistance in a magnetic topological insulator. *Phys. Rev. Lett.* **117**, 127202 (2016).
12. Godinho, J. et al. Electrically induced and detected Néel vector reversal in a collinear antiferromagnet. *Nat. Commun.* **9**, 4686 (2018).

13. Ma, Q. et al. Observation of the nonlinear Hall effect under time-reversal-symmetric conditions. *Nature* **565**, 337–342 (2019).
14. Kang, K., Li, T., Sohn, E., Shan, J. & Mak, K. F. Nonlinear anomalous Hall effect in few-layer WTe_2. *Nat. Mater.* **18**, 324–328 (2019).
15. Kumar, D. et al. Room-temperature nonlinear Hall effect and wireless radiofrequency rectification in Weyl semimetal $TaIrTe_4$. *Nat. Nanotechnol.* **16**, 421–425 (2021).
16. Isobe, H., Xu, S.-Y. & Fu, L. High-frequency rectification via chiral Bloch electrons. *Sci. Adv.* **6**, eaay2497 (2020).
17. Zhao, W. et al. Magnetic proximity and nonreciprocal current switching in a monolayer WTe_2 helical edge. *Nat. Mater.* **19**, 503–507 (2020).
18. Tsirkin, S. & Souza, I. On the separation of Hall and ohmic nonlinear responses. *SciPost Phys. Core* **5**, 039 (2022).
19. He, P. et al. Graphene moiré superlattices with giant quantum nonlinearity of chiral Bloch electrons. *Nat. Nanotechnol.* **17**, 378–383 (2022).
20. Zhang, Z. et al. Non-reciprocal charge transport in an intrinsic magnetic topological insulator $MnBi_2Te_4$. *Nat. Commun.* **13**, 6191 (2022).
21. Wu, H. et al. The field-free Josephson diode in a van der Waals heterostructure. *Nature* **604**, 653–656 (2022).
22. Gao, A. et al. Quantum metric nonlinear Hall effect in a topological antiferromagnetic heterostructure. *Science* **381**, 181–186 (2023).
23. Wang, N. et al. Quantum-metric-induced nonlinear transport in a topological antiferromagnet. *Nature* **621**, 487–492 (2023).
24. Zhang, C.-P., Gao, X.-J., Xie, Y.-M., Po, H. C. & Law, K. T. Higher-order nonlinear anomalous Hall effects induced by Berry curvature multipoles. *Phys. Rev. B* **107**, 115142 (2023).
25. Wang, C., Gao, Y. & Xiao, D. Intrinsic nonlinear Hall effect in antiferromagnetic tetragonal CuMnAs. *Phys. Rev. Lett.* **127**, 277201 (2021).
26. Liu, H. et al. Intrinsic second-order anomalous Hall effect and its application in compensated anti-ferromagnets. *Phys. Rev. Lett.* **127**, 277202 (2021).
27. Holder, T., Kaplan, D., Ilan, R. & Yan, B. Mixed axial-gravitational anomaly from emergent curved spacetime in nonlinear charge transport. Preprint at https://arxiv.org/abs/2111.07780 (2021).
28. Lahiri, S., Das, K., Culcer, D. & Agarwal, A. Intrinsic nonlinear conductivity induced by the quantum metric dipole. *Phys. Rev. B* **108**, L201405 (2023).
29. Smith, T. B., Pullasseri, L. & Srivastava, A. Momentum-space gravity from the quantum geometry and entropy of Bloch electrons. *Phys. Rev. Res.* **4**, 013217 (2022).
30. Ma, D., Arora, A., Vignale, G. & Song, J. C. Anomalous skew-scattering nonlinear Hall effect and chiral photocurrents in $\mathcal{PT}$-symmetric antiferromagnets. *Phys. Rev. Lett.* **131**, 076601 (2023).
31. Zhang, N. J. et al. Angle-resolved transport non-reciprocity and spontaneous symmetry breaking in twisted trilayer graphene. *Nat. Mater.* **23**, 356–362 (2024).
32. Kaplan, D., Holder, T. & Yan, B. Unification of nonlinear anomalous Hall effect and nonreciprocal magnetoresistance in metals by the quantum geometry. *Phys. Rev. Lett.* **132**, 026301 (2024).
33. Huang, Y.-X. et al. Nonlinear current response of two-dimensional systems under in-plane magnetic field. *Phys. Rev. B* **108**, 075155 (2023).
34. Huang, Y.-X., Xiao, C., Yang, S. & Li, X. Scaling law for time-reversal-odd nonlinear transport. Preprint at https://arxiv.org/abs/2311.01219 (2023).
35. Atencia, R. B., Xiao, D. & Culcer, D. Disorder in the non-linear anomalous Hall effect of $\mathcal{PT}$-symmetric Dirac fermions. *Phys. Rev. B* **108**, L201115 (2023).
36. Kaplan, D., Holder, T. & Yan, B. General nonlinear Hall current in magnetic insulators beyond the quantum anomalous Hall effect. *Nat. Commun.* **14**, 3053 (2023).
37. Otrokov, M. M. et al. Prediction and observation of an antiferromagnetic topological insulator. *Nature* **576**, 416–422 (2019).
38. Deng, Y. et al. Quantum anomalous Hall effect in intrinsic magnetic topological insulator $MnBi_2Te_4$. *Science* **367**, 895–900 (2020).
39. Liu, C. et al. Robust axion insulator and Chern insulator phases in a two-dimensional antiferromagnetic topological insulator. *Nat. Mater.* **19**, 522–527 (2020).
40. Trang, C. X. et al. Crossover from 2D ferromagnetic insulator to wide bandgap quantum anomalous Hall insulator in ultra-thin $MnBi_2Te_4$. *ACS Nano* **15**, 13444–13452 (2021).
41. Deng, H. et al. High-temperature quantum anomalous Hall regime in a $MnBi_2Te_4/Bi_2Te_3$ superlattice. *Nat. Phys.* **17**, 36–42 (2021).
42. Gao, A. et al. Layer Hall effect in a 2D topological axion antiferromagnet. *Nature* **595**, 521–525 (2021).
43. Cai, J. et al. Electric control of a canted-antiferromagnetic Chern insulator. *Nat. Commun.* **13**, 1668 (2022).
44. Beidenkopf, H. et al. Spatial fluctuations of helical Dirac fermions on the surface of topological insulators. *Nat. Phys.* **7**, 939–943 (2011).
45. Qiu, J.-X. et al. Axion optical induction of antiferromagnetic order. *Nat. Mater.* **22**, 583–590 (2023).
46. Iyama, A. & Kimura, T. Magnetoelectric hysteresis loops in Cr_2O_3 at room temperature. *Phys. Rev. B* **87**, 180408 (2013).
47. Ahn, J., Xu, S.-Y. & Vishwanath, A. Theory of optical axion electrodynamics and application to the Kerr effect in topological antiferromagnets. *Nat. Commun.* **13**, 7615 (2022).
48. Fujimoto, T. et al. Observation of terahertz spin Hall conductivity spectrum in GaAs with optical spin injection. *Phys. Rev. Lett.* **132**, 016301 (2023).
49. Orenstein, J. Optical nonreciprocity in magnetic structures related to high-T_c superconductors. *Phys. Rev. Lett.* **107**, 067002 (2011).
50. Varma, C. Gyrotropic birefringence in the underdoped cuprates. *Europhys. Lett.* **106**, 27001 (2014).
51. Yan, J.-Q. et al. Crystal growth and magnetic structure of $MnBi_2Te_4$. *Phys. Rev. Mater.* **3**, 064202 (2019).
52. Hsieh, D. et al. Selective probing of photoinduced charge and spin dynamics in the bulk and surface of a topological insulator. *Phys. Rev. Lett.* **107**, 077401 (2011).
53. Vool, U. et al. Imaging phonon-mediated hydrodynamic flow in WTe_2. *Nat. Phys.* **17**, 1216–1220 (2021).
54. Thiel, L. et al. Probing magnetism in 2D materials at the nanoscale with single-spin microscopy. *Science* **364**, 973–976 (2019).
55. Steiner, S., Khmelevskyi, S., Marsmann, M. & Kresse, G. Calculation of the magnetic anisotropy with projected-augmented-wave methodology and the case study of disordered $Fe_{1-x}Co_x$ alloys. *Phys. Rev. B* **93**, 224425 (2016).
56. Perdew, J. P. et al. Generalized gradient approximation made simple. *Phys. Rev. Lett.* **77**, 3865–3868 (1996).
57. Pizzi, G. et al. Wannier90 as a community code: new features and applications. *J. Phys.: Condens. Matter* **32**, 165902 (2020).

Acknowledgements

We thank Y. Gao, C. Xiao, A. Agarwal, J. Ahn, S. Yang, F. de Juan and I. Sodemann for helpful discussions. The work in S.Y.X.'s group was partly supported through the Center for the Advancement of Topological Semimetals, an Energy Frontier Research Center funded by the US Department of Energy (DOE), Office of Science (fabrication and measurements), through the Ames National Laboratory (Contract

No. DE-AC-0207CH11358) and partly through the Air Force Office of Scientific Research (Grant No. FA9550-23-1-0040 for data analysis and manuscript writing). S.Y.X. acknowledges the Corning Fund for Faculty Development and support from the Alfred P. Sloan Foundation. S.Y.X. and D.B. were supported by the National Science Foundation (NSF; Career Grant No. DMR-2143177). C.T. and Z.S. acknowledge support from the Swiss National Science Foundation (Project Nos. P2EZP2 191801 and P500PT 206914, respectively). Y.F.L., S.Y.X., D.C.B., Y.O. and L.F. were supported by the Science and Technology Center for Integrated Quantum Materials (NSF Grant No. DMR-1231319). This work was performed in part at the Center for Nanoscale Systems, Harvard University, a member of the National Nanotechnology Coordinated Infrastructure Network, which is supported by the NSF (Award No. ECCS-2025158). Bulk single-crystal growth and characterization of $MnBi_2Te_4$ were performed at the University of California, Los Angeles, and were supported by the DOE, Office of Science (Award No. DE-SC0021117). The work at Northeastern University was supported by the NSF through NSF-ExpandQISE (Award No. 2329067), and it benefited from the resources of Northeastern University's Advanced Scientific Computation Center and the Discovery Cluster and of the Quantum Materials and Sensing Institute. The work in Q.M.'s group was supported through the Center for the Advancement of Topological Semimetals, an Energy Frontier Research Center funded by the DOE, Office of Science, through the Ames National Laboratory (Contract No. DE-AC02-07CH11358 for sample fabrication) and was partly supported by the Air Force Office of Scientific Research (Grant No. FA9550-22-1-0270 for manuscript writing) and the Alfred P. Sloan Foundation. L.F. and Q.M. also acknowledge support from the NSF Convergence programme (NSF ITE-2345084) and the Canadian Institute for Advanced Research. T.R.C. was supported by the 2030 Cross-Generation Young Scholars Programme from the National Science and Technology Council, Taiwan (Programme No. MOST111-2628-M-006-003-MY3), National Cheng Kung University, Taiwan, and the National Center for Theoretical Sciences, Taiwan. T.R.C. thanks the National Center for High-performance Computing of the National Applied Research Laboratories, Taiwan, for providing computational and storage resources. This research was supported, in part, by the Higher Education Sprout Project, Ministry of Education, to the Headquarters of University Advancement at National Cheng Kung University. H.L. acknowledges the support of the National Science and Technology Council, Taiwan (Grant No. MOST 111-2112-M-001-057-MY3). The work at the Tata Institute of Fundamental Research, Mumbai, was supported by the Department of Atomic Energy of the Government of India (Project No. 12-R&D-TFR-5.10-0100) and benefited from the computational resources of the Tata Institute of Fundamental Research, Mumbai. K.W. and T.T. acknowledge support from the JSPS KAKENHI (Grant Nos. 21H05233 and 23H02052) and World Premier International Research Center Initiative (WPI), MEXT, Japan. S.W.C. acknowledges partial support from the Harvard Quantum Initiative in Science and Engineering.

Author contributions

S.Y.X. conceived and supervised the project. A.G. fabricated the devices and performed the transport measurements with help from Y.F.L., J.X.Q., D.B., T.D., H.C.L., C.T., Z.S., S.C.H., T.H., D.C.B. and Q.M. A.G., S.W.C. and S.P. performed the microwave rectification and NV experiments with help from A.Y. A.G. and J.X.Q. performed the optical CD measurement. A.G. performed the SHG measurements with help from C.T., H.C.L., J.X.Q. and Y.F.L. C.H., T.Q. and N.N. grew the bulk $MnBi_2Te_4$ single crystals. B.G. completed the theoretical studies including first-principles calculations with help from Y.O. and under the guidance of B.S., A.B., H.L., L.F. and T.R.C. K.W. and T.T. grew the bulk h-BN single crystals. S.Y.X., A.G. and Q.M. wrote the manuscript with input from all authors.

Competing interests

The authors declare no competing interests.

Additional information

Extended data is available for this paper at https://doi.org/10.1038/s41928-024-01219-8.

Supplementary information The online version contains supplementary material available at https://doi.org/10.1038/s41928-024-01219-8.

Correspondence and requests for materials should be addressed to Su-Yang Xu.

Peer review information *Nature Electronics* thanks the anonymous reviewers for their contribution to the peer review of this work.

Reprints and permissions information is available at www.nature.com/reprints.

Publisher's note Springer Nature remains neutral with regard to jurisdictional claims in published maps and institutional affiliations.

Springer Nature or its licensor (e.g. a society or other partner) holds exclusive rights to this article under a publishing agreement with the author(s) or other rightsholder(s); author self-archiving of the accepted manuscript version of this article is solely governed by the terms of such publishing agreement and applicable law.

© The Author(s), under exclusive licence to Springer Nature Limited 2024

https://doi.org/10.1038/s41928-024-01219-8

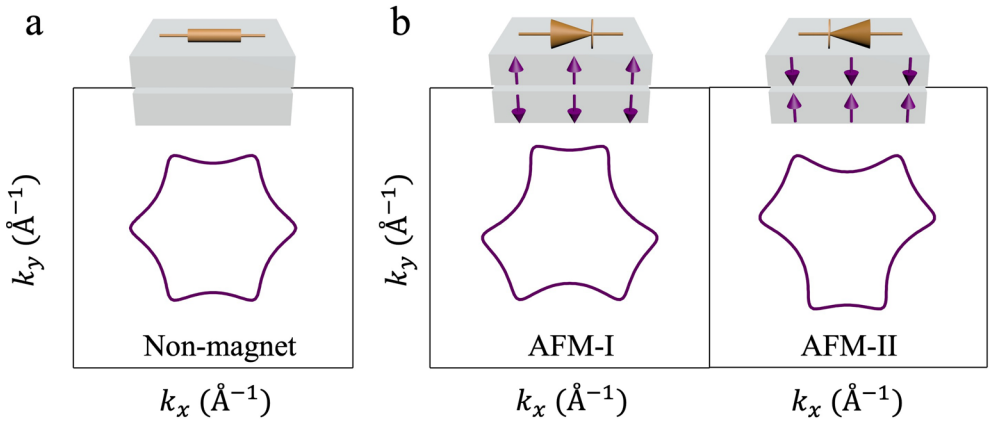

Extended Data Fig. 1 | The asymmetric band contours induced by AFM spins in 6SL $MnBi_2Te_4$ at Fermi energy E_f = 0.2 eV. a, The band contours of the Dirac surface states without AFM order. The band contour is symmetric for momentum ± *k*. ± k_x and ± k_y are the momentum along x and y direction. **b**, The band contours of the Dirac surface states for opposite AFM states. The AFM spins make the band to be ± k_y asymmetric. This AFM spin-induced asymmetry is opposite for opposite AFM states. This explains the observation that the AFM diode effect signal is opposite for opposite AFM states shown in Figs. 2e–f, 4f and Extended Data Fig. 4.

https://doi.org/10.1038/s41928-024-01219-8

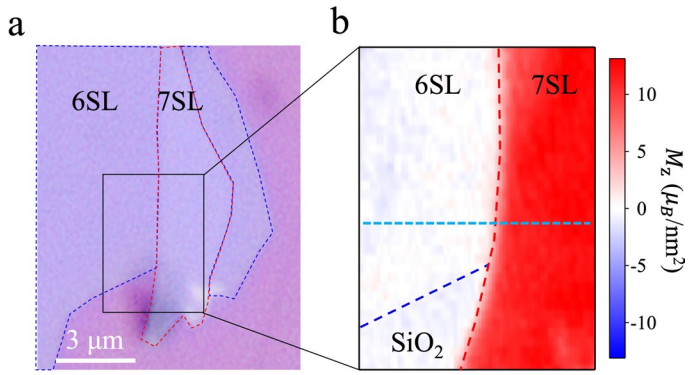

Extended Data Fig. 2 | The fully compensated antiferromagnetism for 6SL $MnBi_2Te_4$. a, b, NV center magnetometry measurement for even- and odd-layered $MnBi_2Te_4$ (outlined by blue and red dashed lines in the optical image of the sample in (**a**)). The magnetization is only observed in odd-layered $MnBi_2Te_4$ and negligible in even-layered $MnBi_2Te_4$. The cyan dotted line denotes the line cut data shown in Fig. 1e.

https://doi.org/10.1038/s41928-024-01219-8

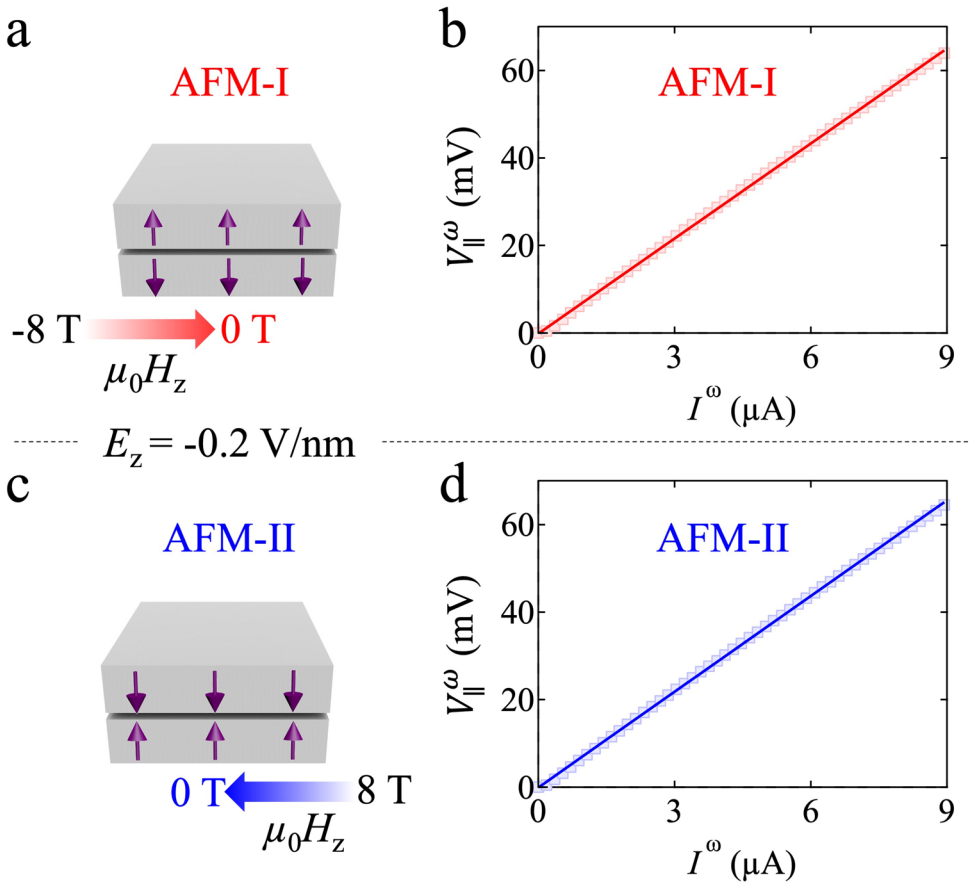

Extended Data Fig. 3 | The linear and nonlinear signals for opposite AFM states in a 6SL $MnBi_2Te_4$. a, c, At a finite external magnetic field $\mu_0 H_z$ field, AFM-I state can be prepared by sweeping $\mu_0 H_z$ from -8 T to 0 T (panel **a**); AFM-II state can be prepared by sweeping $\mu_0 H_z$ from +8 T to 0 T (panel **c**). **b**, The linear longitudinal voltage $V_{\parallel}^{\omega}$ as a function of injection current for AFM-I. **d,** Same as (panel **b**) but for AFM-II. For different AFM states, the linear signal is the same. These data were taken from Device A and the current was along 30° in Fig. 2g.

https://doi.org/10.1038/s41928-024-01219-8

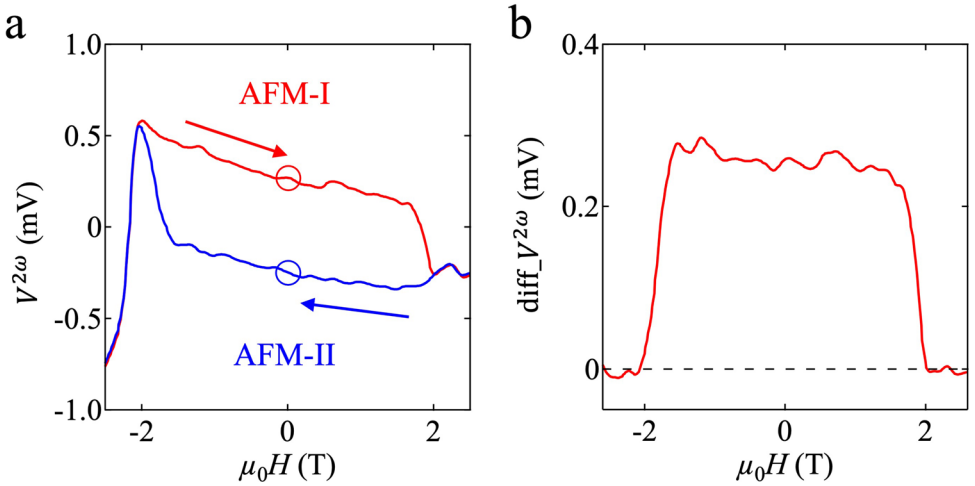

Extended Data Fig. 4 | AFM order determined nonlinear signal. a, Nonlinear voltage $V^{2\omega}$ as a function of z-direction external magnetic field $\mu_0 H_z$. $V^{2\omega}$ is opposite for two AFM orders ($|\mu_0 H| < 2$ T). The red and blue circles denote the two opposite $V^{2\omega}$ at $\mu_0 H = 0$ T. **b**, The nonlinear voltage difference ($\mathrm{diff}_{V^{2\omega}} = \frac{1}{2}(V^{2\omega}_{\mathrm{AFM-I}} - V^{2\omega}_{\mathrm{AFM-II}})$) between two AFM orders as a function of $\mu_0 H$.

https://doi.org/10.1038/s41928-024-01219-8

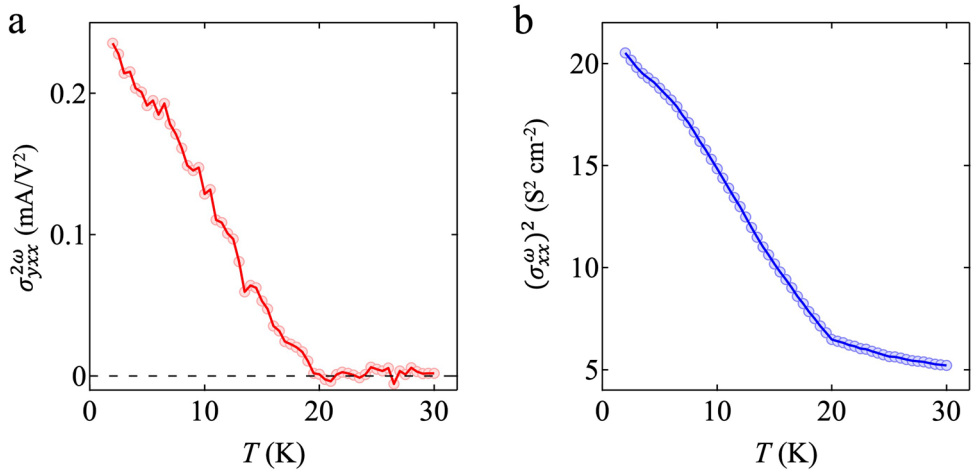

Extended Data Fig. 5 | The temperature dependence of the nonlinear signal. a, b, Nonlinear conductivity $V^{2\omega}_{yxx}$ and square of linear conductivity $(\sigma^{\omega}_{xx})^2$ as a function of temperature. $\sigma^{2\omega}_{yxx}$ and $(\sigma^{\omega}_{xx})^2$ show a similar temperature dependence.

https://doi.org/10.1038/s41928-024-01219-8

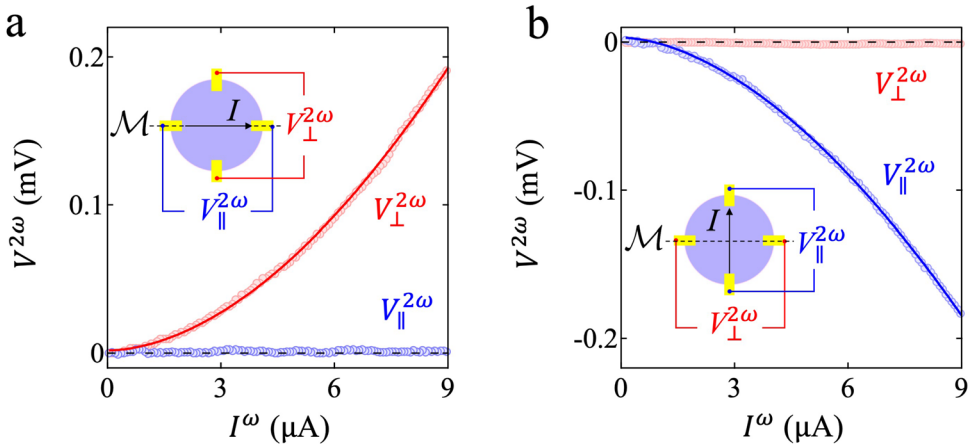

Extended Data Fig. 6 | Nonlinear voltage versus current direction. a, b, Longitudinal and transverse nonlinear voltage when the current is injected along *x* (panel **a**) and along y (panel **b**). A crystalline axes is along *x* in Device A (Fig. 2g,h).

https://doi.org/10.1038/s41928-024-01219-8

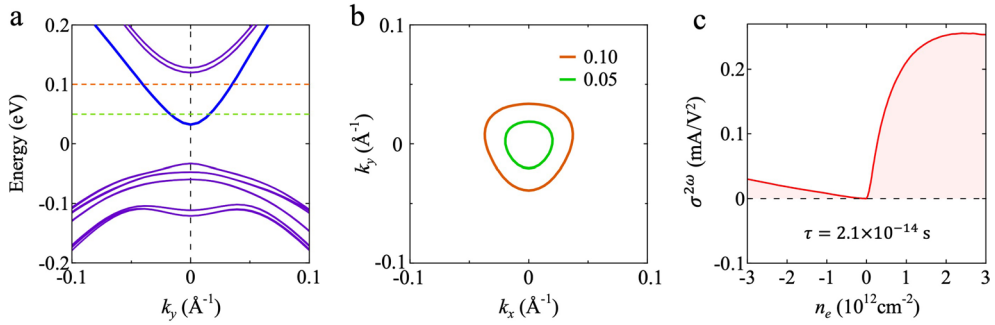

Extended Data Fig. 7 | DFT calculated band structure of 6SL $MnBi_2Te_4$. **a**, Band structure of 6SL $MnBi_2Te_4$ in k_y direction. **b**, DFT calculated band contours at specific energies (0.05 eV and 0.10 eV), marked with dashed lines in panel (**a**). The low energy Dirac bands show dramatic asymmetry between + k_y and − k_y. **c**, DFT calculated nonlinear conductivity $\sigma^{2\omega}$ as a function of Fermi level E_f. We obtained the relaxation time $\tau = 2.1 \times 10^{-14}$ s based on the Drude conductivity. We note that our calculations are based on the DFT band structure of 6SL $MnBi_2Te_4$, which predicts a magnetic gap ~ 50 meV. However, experimentally, the gap size is not settled[37,40]. In particular, spatial inhomogeneity can smear out the magnetic gap[44]. Moreover, the antisite defects could suppress the band gap and can increase the quantum metric effect, as predicted in Ref. 32.

https://doi.org/10.1038/s41928-024-01219-8

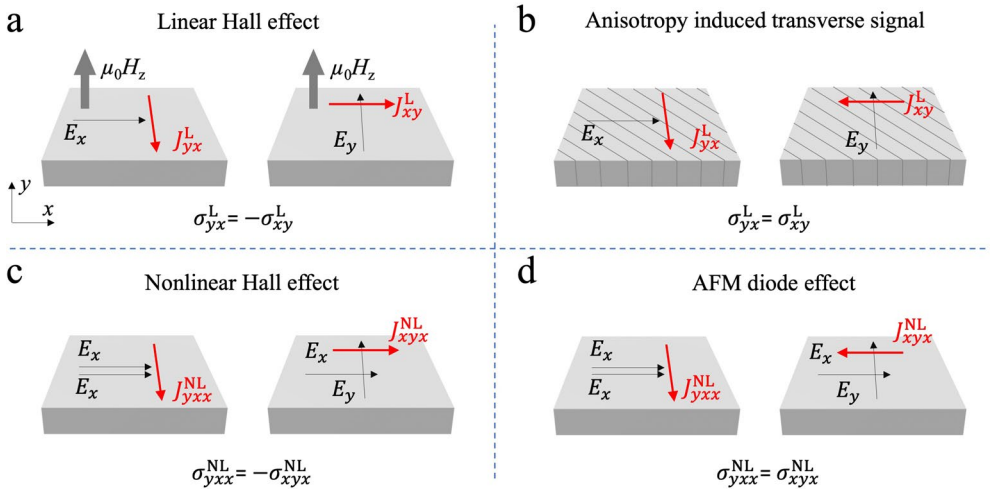

Extended Data Fig. 8 | The exchange property of transverse conductance. **a, b**, Schematics of two different types of linear transverse conductance, the Hall effect (panel **a**) and the anisotropy induced transverse signal (panel **b**). The Hall effect occurs due to external magnetic field or internal magnetization. The anisotropy induced transverse signal occurs due to crystalline anisotropy (for example orthorhombic or monoclinic). These two different mechanisms can be distinguished by their exchange properties. The Hall effect is antisymmetric ($\sigma_{xy} = -\sigma_{yx}$), whereas the anisotropy induce transverse signal is symmetric ($\sigma_{xy} = \sigma_{yx}$). **c, d**, Schematic of nonlinear Hall signal (panel **c**) and the transverse component of the AFM diode signal (panel **d**). The nonlinear Hall signal is antisymmetric ($\sigma_{yxx} = -\sigma_{xyx}$), while the AFM diode signal is symmetric ($\sigma_{yxx} = \sigma_{xyx}$).

https://doi.org/10.1038/s41928-024-01219-8

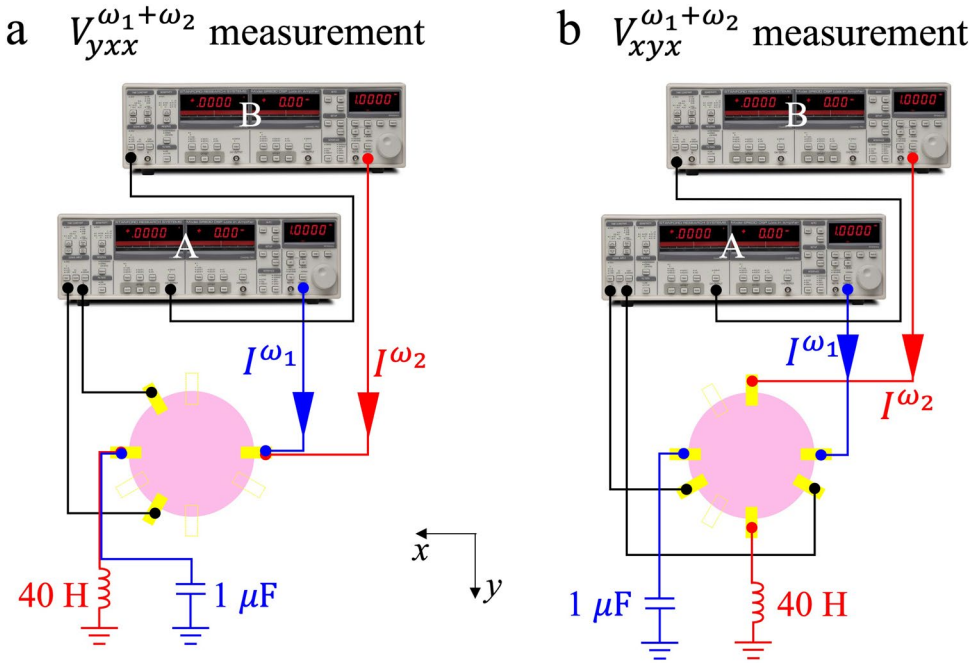

Extended Data Fig. 9 | Electrical sum-frequency generation (SFG) measurement for 6SL $MnBi_2Te_4$. a, b, Schematic for $V_{yxx}^{\omega_1+\omega_2}$ and $V_{xyx}^{\omega_1+\omega_2}$ measurements, respectively. ω_1 = 547.1 Hz and ω_2 = 1.77 Hz were used in the measurement. The capacitor and inductor were used to define the current trajectory for I^{ω_1} and I^{ω_2} (see Methods for more details).

https://doi.org/10.1038/s41928-024-01219-8

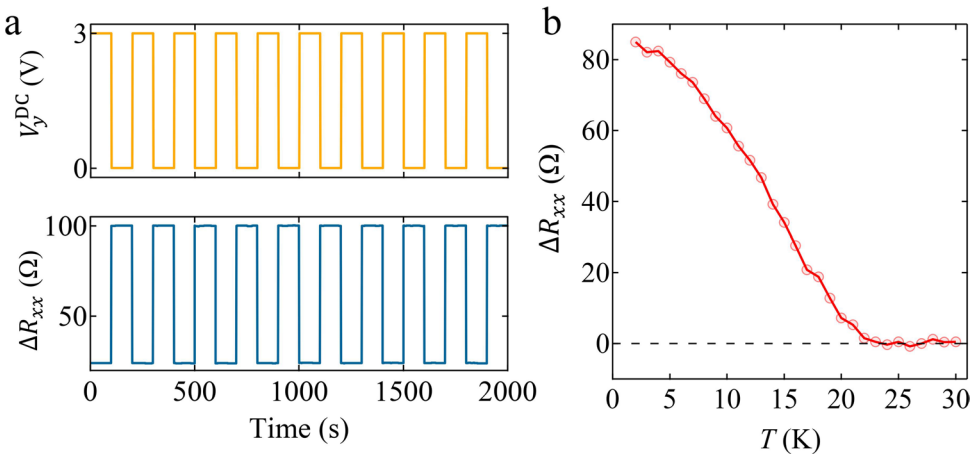

Extended Data Fig. 10 | In-plane field effect in another 6SL $MnBi_2Te_4$ device. a, Measured change of resistance R_{xx}($\Delta R_{xx} = V_x^{\omega_1}/I_x^{\omega_1}$) as a function of an electric field bias along V_y^{DC}. **b**, Temperature dependence of ΔR_{xx}.